Simultaneous boundary-layer transition, tip vortex, and blade deformation measurements of a rotor in hover

James Heineck
Photographic Technologist
NASA Ames Research Center
Moffett Field, CA, USA

Edward Schairer
Aerospace Engineer
NASA Ames Research Center
Moffett Field, CA, USA

Manikandan Ramasamy
Aerospace Engineer
U.S. Army
Moffett Field, CA, USA

Nettie Roozeboom
Aerospace Engineer
NASA Ames Research Center
Moffett Field, CA, USA

ABSTRACT

This paper describes simultaneous optical measurements of a sub-scale helicopter rotor in the U.S. Army Hover Chamber at NASA Ames Research Center. The measurements included thermal imaging of the rotor blades to detect boundary layer transition; retro-reflective background-oriented schlieren (RBOS) to visualize vortices; and stereo photogrammetry to measure displacements of the rotor blades, to compute spatial coordinates of the vortices from the RBOS data, and to map the thermal imaging data to a three-dimensional surface grid. The test also included an exploratory effort to measure flow near the rotor tip by tomographic particle image velocimetry (tomo PIV)—an effort that yielded valuable experience but little data. The thermal imaging was accomplished using an image-derotation method that allowed long integration times without image blur. By mapping the thermal image data to a surface grid it was possible to accurately locate transition in spatial coordinates along the length of the rotor blade.

NOTATION

ω_R	rotational frequency of the rotor
ω_M	rotational frequency of the tracking mirror
X, Y	image-plane coordinates
x, y, z	object-space coordinates (z vertical, positive down)
L	DLT coefficients
Θ	Pitch angle of blade
R	Spanwise location on the blade
x	chordwise location on the blade

INTRODUCTION

Thermography has been used for detecting boundary layer transition on fixed-wing airfoils since the mid 1980's. References 1-3 are a small subset of experiments in the literature. Integration times for these measurements were relatively long – several milliseconds. New camera technology has given rise to new applications for transition detection, including rotating airfoils. While one-per-rev synchronization along with significant improvements in resolution and image quality open the possibility for full-scale in-flight measurements on helicopter blades, a major hurdle for the rotating-wing airfoil has been image blur caused by blade motion during the long integration time. A corrective method based on image derotation for tracking rotor blade using imaging devices with long integration times r has been developed (Ref 4). Applications for derotation method include PSP, TSP, thermography, and tuft imaging.

Figure 1 is an illustration of the de-rotation concept, where a mirror with a long aspect ratio is mounted on a driven with a servo-motor. A one-per-rev timing pulse from the rotor system is used by the motor controller that halves the input frequency to set the mirror rpm (ω_M) to ½ that of the rotor rpm (ω_R). The camera views the reflection of the rotor disk, such that a blade will remain still on the camera sensor regardless of its angular travel. The reflection included angle changes twice as fast as the mirror's rotation angle, thus by halving the mirror's rotation relative to the rotor's rotation, the reflected image remains fixed.

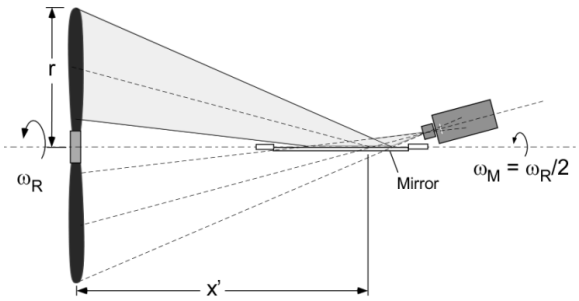

Figure 1. Diagram of image de-rotation concept

The result of permitting the image of the blade to dwell in the sensor in this fashion is an unblurred, properly exposed thermal image of the blade surface. Boundary layer transition is shown as a change in gray scale due to turbulent mixing of ambient air with a significant temperature differential from the blade surface.

Presented at the AHS Technical Meeting on Aeromechanics Design for Vertical Lift, San Francisco, CA, January 20-22, 2016. Copyright © 2016 by the American Helicopter Society International, Inc. All rights reserved.

The initial goal of this experiment was to acquire four different imaging-based measurements simultaneously on and around the rotor on a one-per-rev basis. The techniques deployed included Tomographic PIV, Retroreflective Background Oriented Schlieren (RBOS), Blade Deformation Photogrammetry, and Thermography. The intent was to prove that all of these methods can be used simultaneously without "light contamination" from one method to the other. This was demonstrated, however calibration errors for the PIV prevented the presentation of results from all of these techniques. This experiment follows an effort at DLR Goettingen with Raffel and Mulleners where PIV, RBOS and Blade photogrammetry were acquired on a similarly sized rotor. The following discusses the thermography, RBOS and Blade Displacement photogrammetry, and, using techniques developed for Pressure Sensitive Paint measurements, the use of that calibration for the thermal imagery mapping method.

EXPERIMENTAL SET-UP

Experiments were conducted on a two-bladed rotor system at the U. S. Army hover chamber (25- by 25- by 30-ft high) located at NASA Ames Research Center. Such a large testing volume ensured that the recirculation effects were minimal. Rotor blades were untwisted and had rectangular planform with NACA 0012 airfoil throughout the span. The radius and chord of the rotor blades were 2.97 ft and 2.55 inches, respectively. The rotor hub plane was 10 ft above the ground and was spun thrusting down with the lifting surface of the blade facing the ground. This allowed convenient placement and control of various cameras and mirrors to focus on the suction side of the blade where transition needs to be studied.

The rotor system was equipped with swash plate and servo controls to change the collective and cyclic pitches. All the experiments were conducted in hover condition, i.e., only collective pitch was varied. Measurements were made at three different pitch settings (3 deg, 6 deg, and 9 deg) and at a rotational speed of 900 rpm. A Hall-effect sensor was used to acquire 1/rev signal that was later used to synchronize the mirror. The rotor system was equipped with an electronic speed controller that ensured minimal variation of rpm (within 1 rpm) during acquisition. A pair of accelerometers attached to the stand measured the system vibration for safe operation. The rotors were tracked and dynamically balanced using a digital signal analyzer.

Thermography

The thermal imaging camera was a FLIR SC8250 camera with a 1k x 1k pixel InSb sensor. The camera was externally synchronized with the mirror using a Hall-effect signal generator mounted on the frame of the mirror. The mirror was rotated using a Compumotor high-inertia type servo motor with 113 lb-in (12.8 Nm) of torque and 5000 rpm maximum. The motor controller permitted the acceptance of the one-per-rev pulse from the rotor and used this signal to set the mirror rotational frequency. The entire mirror and camera assembly was mounted on a traverse driven frame that allowed the operator to adjust the pointing angle and overall position of the camera/mirror to optimize the image composition and the location of the mirror's rotational axis. It is necessary to collocate the axis of rotation of the mirror to the center of rotation of the rotor disk to achieve the sharpest possible focus.

In addition to the imager and mirror system, 2 one kilowatt tungsten light source were mounted to the fixed frame near the rotor to act as heaters for the blades. The ambient temperature of the Chamber could not be controlled, as is the case in many wind tunnels. So the temperature differential necessary to show the turbulent mixing had to be induced by heating the blade surface. Passive recording was attempted but the contrast was too low.

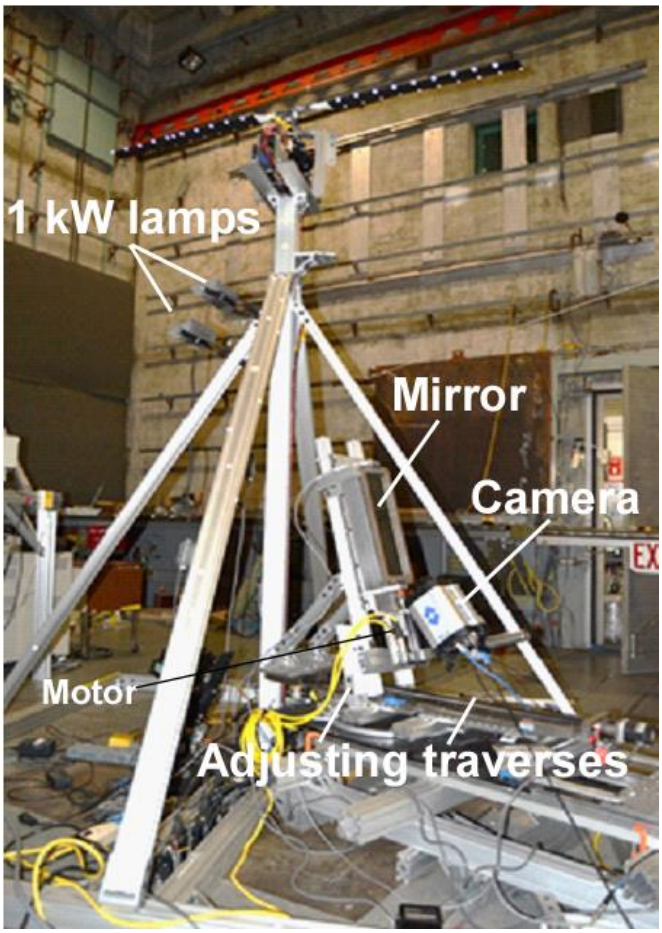

Figure 2. Overview of the thermal imaging system and the rotor test stand.

The camera exposure time was 4.5 milliseconds, during which time the rotor moved 24 deg. Figure 3 shows raw thermal images of the rotor blade at 900 rpm with a collective of 3 *deg.* The rotational direction is from bottom to top of the image. The top image was recorded without heating (passively) and the bottowm image shows the effects of heating. Here, the warm blade (bright area) is cooled by the relatively cool turbulence from the ambient air (darker regions). The streak of highlight behind the root of the blade of the heated blade a light on the ceiling. The dots were fiducials for the blade displacement measurements and were thick enough to trip the boundary layer.

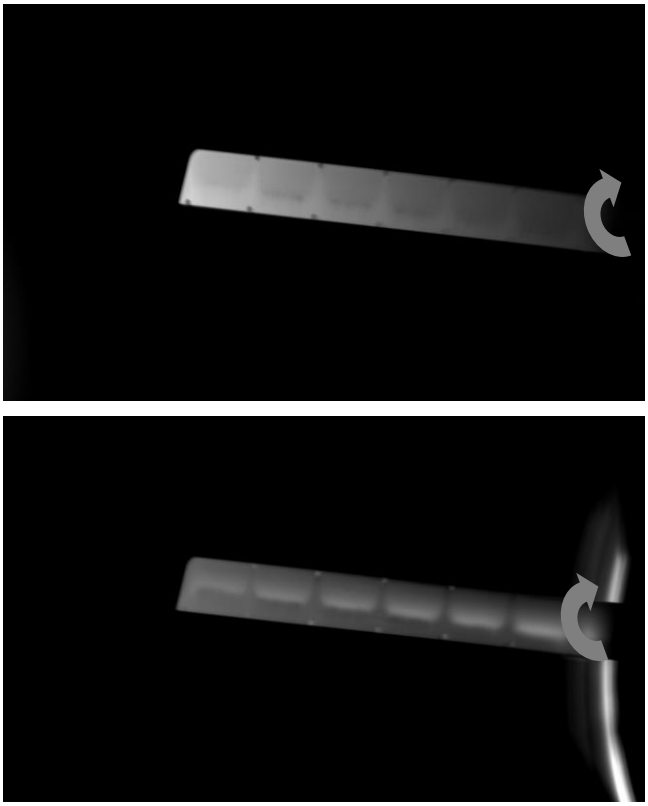

Figure 3. Cropped raw thermal images in grayscale of a blade at 900 rpm and 3 deg collective. Top was passively recorded, bottom was recorded during blade heating.

Photogrammetry/RBOS

The concept for the experiment was to use a single set of stereo photogrammetry cameras to simultaneously measure the positions of vortex filaments shed from the tips of the rotor blades and the positions of the blades themselves. The measurements were made at a single blade azimuth angle. Blade displacements were measured by tracking retro-reflective targets along the leading and trailing edges of the blades. Vortex filaments were measured in the same images by a three-step procedure: 1. RBOS was used to visualize the filaments; 2. epipolar geometry was used to locate corresponding points on each filament in the stereo images; and 3. stereo photogrammetry was used to compute the spatial positions of the corresponding points.

Three Dalsa 4M15 cameras (2k x 2k pixels) were placed on the floor of the test chamber looking upwards at the suction surfaces of the downward-thrusting rotor blades (Fig. 4). The cameras were positioned along a line radiating outward from the mast at the selected azimuth angle so that the line between them was perpendicular to the largely circumferential vortex filaments. This was best for applying epipolar geometry.

A speckled retro-reflective panel served as a background for each camera view. Each panel consisted of a plywood backing to which a sheet of 3M 900X retro-reflective material with adhesive backing was applied. Speckles were produced by splattering the retro-reflector surface with black paint using a pressurized spray gun that was "de-tuned" to

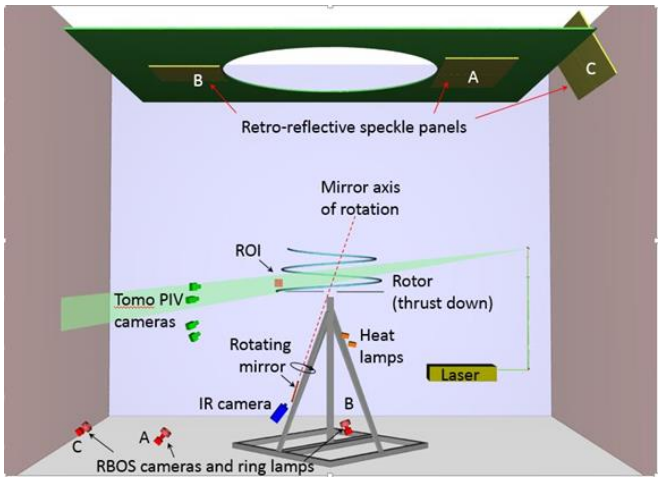

Figure 4. Schematic showing layout of instruments.

produce droplets rather than a fine mist. Two horizontal panels (A and B), each 48 x 48 in, were secured with screws to the false ceiling of the test chamber, one on each side of a large circular opening that reduced blockage of vertical airflow; a third, larger, panel (C, 72-in wide by 48-in high) was mounted to one wall and was tilted downward approximately 30° from vertical to reduce the angle between its surface normal and the optical axis of the third camera.

A ring flash-lamp composed of high-intensity red LEDs was co-located with each camera. The intensity of light returned from the retro-reflective panels to the cameras was diminished because the panels were not perpendicular to the incident light. The cameras were focused on the background panels and f-stops were set to 8 to provide good depth-of-field. The cameras and flash lamps were triggered by a TTL square-wave from a digital signal generator that was synchronized to a once-per-rev signal from an encoder on the rotor mast. The flash durations of the lamps were set to obtain satisfactory images of the speckled background from the cameras. Two of the lamps (A and B in Fig. 1) were of the same type, and their flash duration (550 µsec) was set by the duty cycle of the square wave, which was adjusted at the signal generator. The duration of the flash from the third lamp (C in Figure 4) was set at the lamp control box and was much shorter—10 µsec. A shorter exposure was possible for this camera because the lamp was brighter and optical axis of the camera was more nearly perpendicular to the retro-reflective panel than for the other two cameras, so the light returned was greater.

The cameras were calibrated by mounting on the test stand a structure with many targets that filled the volume of space that the rotor blades inhabited at the selected azimuth during testing (Figure. 5). The spatial coordinates of the targets were measured by acquiring images from many directions using a commercial photogrammetry system (VSTARS 2). Then images of the structure were acquired with the floor-mounted photogrammetry cameras and the targets were located in each image. Finally, the Direct Linear Transformation3 (DLT) for each camera was computed from the image- and object-space coordinates of the calibration

targets. The DLT provides the transformation from object-space (x, y, z) to image-plane (X, Y) coordinates:

$$X = \frac{L_1 x + L_2 y + L_3 z + L_4}{L_9 x + L_{10} y + L_{11} z + 1} \quad (1a)$$

$$Y = \frac{L_5 x + L_6 y + L_7 z + L_8}{L_9 x + L_{10} y + L_{11} z + 1} \quad (1b)$$

where L1-L11 are calibration coefficients. With this transformation, the image-plane coordinates of any known spatial point can be computed for a single camera. Computing the spatial coordinates from known image coordinates requires data from at least two cameras (A and B):

$$\begin{bmatrix} X^A L_9^A - L_1^A & X^A L_{10}^A - L_2^A & X^A L_{11}^A - L_3^A \\ Y^A L_9^A - L_5^A & Y^A L_{10}^A - L_6^A & Y^A L_{11}^A - L_7^A \\ X^B L_9^B - L_1^B & X^B L_{10}^B - L_2^B & X^B L_{11}^B - L_3^B \\ Y^B L_9^B - L_5^B & Y^B L_{10}^B - L_6^B & Y^B L_{11}^B - L_7^B \end{bmatrix} \begin{bmatrix} x \\ y \\ z \end{bmatrix} = \begin{bmatrix} L_4^A - X^A \\ L_8^A - Y^A \\ L_4^B - X^B \\ L_8^B - Y^B \end{bmatrix} \quad (2)$$

here superscripts A and B refer to cameras A and B, respectively. This is an over-determined set of linear equations that can be solved in a least-squares sense for (x, y, z). Data for each additional camera adds two equations to the set and usually reduces the error of the least-squares solution.

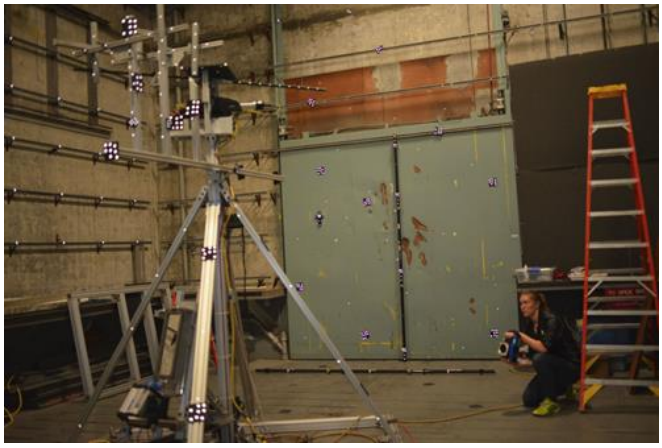

Figure 5. Photo showing calibration structure mounted to test stand. Coded targets were used for VSTARS measurements.

RESULTS

Measurements were made during three runs with the rotor turning at 900 rpm (15 Hz) and with the rotor blade angles set to three, six, and nine degrees.

RBOS

Although RBOS data were acquired at all three rotor-blade pitch angles the weak vortices generated very small optical distortions, thus the data were very noisy and vortices were evident only at the highest angle. Figure 6 shows contour maps of speckle displacements computed by image cross-correlation at each node of a dense grid that overlay the background panel in each image. The data are instantaneous (computed from a single wind-on image from each camera), the correlation window size was 16 x 16 pixels, and the overlap of adjacent windows was 75%. The speckle displacements shown are vertical in the images, which is nearly perpendicular to the filament in each case, and are very small—less than 0.2 pixels. Nonetheless, a vortex filament extending in an arc from the tip of the rotor can be seen in the data from each camera. Additional older vortices from previous blade passages are also visible. When data from more than one blade passage were averaged, the visibility of the youngest vortex was slightly enhanced, but the older, weaker vortices, whose positions were more variable from one blade passage to the next, tended to disappear. Speckle displacements were also measured by two optical-flow methods, one local (ref. 7) and the other global(ref. 8); however, the results were no better than those determined by image cross-correlation.

The youngest vortex filament was approximated by a sequence of 10 points in the data from each camera. Then, for every point on the filament in the data from the first camera (A), an epipolar line was computed for the data from the other two cameras (B and C), and the point of intersection between the epipolar line and the filament was determined for each camera (BA and CA). These points of intersection established the correspondence between vortex points in cameras A and B and cameras A and C. For measurements based on two cameras, vortex points for camera B are simply reassigned to the points of intersection between the vortex and the epipolar lines (B = BA). For three cameras, points in cameras B and C that correspond with a point in camera A (BA and CA) should also correspond with each other. This correspondence, however, is never perfect. Therefore, corresponding points among the three cameras were adjusted to minimize the epipolar errors summed over all points. In Figure 7, images from the three cameras have been overlaid by points defining the vortex filament. The images from cameras B and C include epipolar lines computed from one point in camera A.

In the speckle-displacement data from camera C, two vortex filaments extend from the tip of the rotor blade, and it is not obvious which is the youngest (Figure 6, bottom). This ambiguity was eliminated by applying the epipolar constraints described above: the sum of the epipolar errors was much smaller when the filament that is marked was assumed to be the youngest rather than the other filament. In addition, when spatial coordinates of points on the filament were computed using the marked filament, the error in the least squares solution to Eq. 2 was much smaller than when the other filament was chosen. After correspondence of points on the vortex filaments was been established, the spatial coordinates of the points were computed from Eq. 2. In Figure 8 the vortex has been visualized from above along with the rotor and test stand.

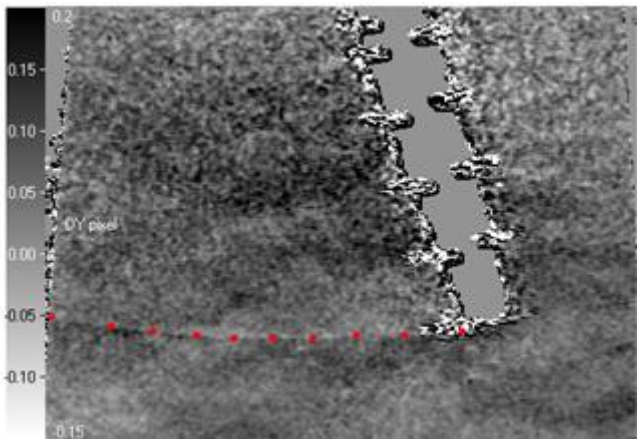

A

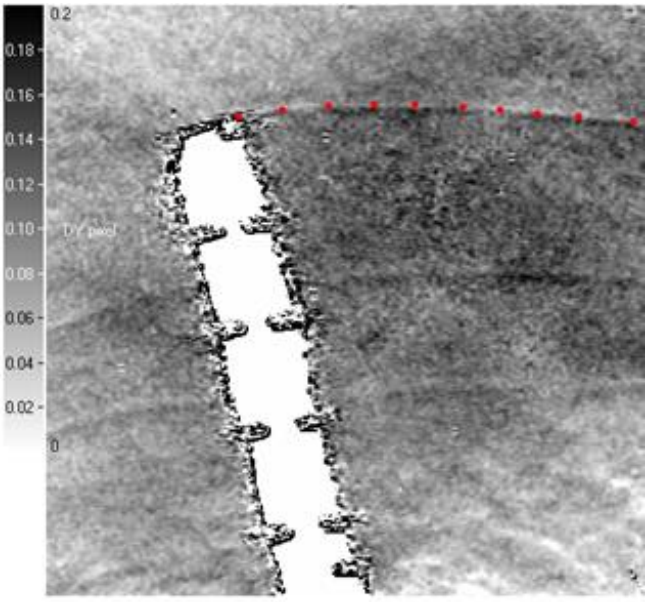

B

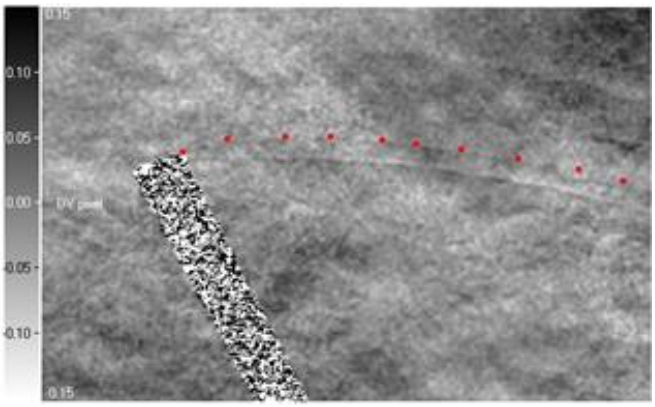

C

Figure 6. Speckle displacement distributions from cameras A (top), B (middle), and C (bottom). RPM = 900, Θ = 9°.

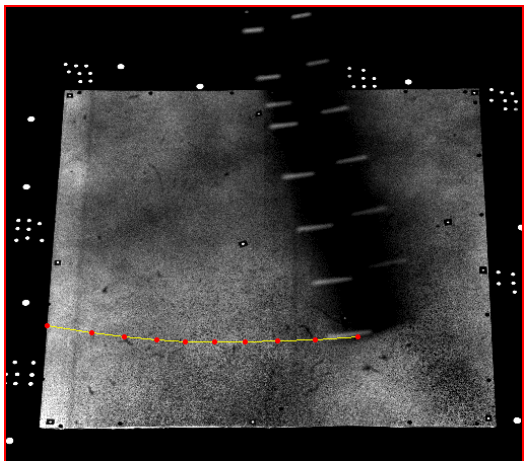

A

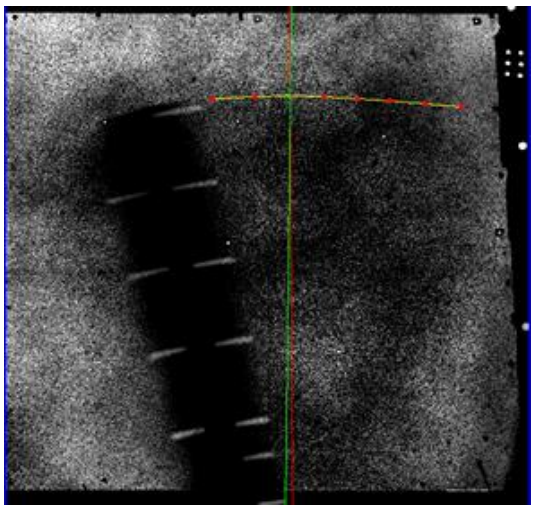

B

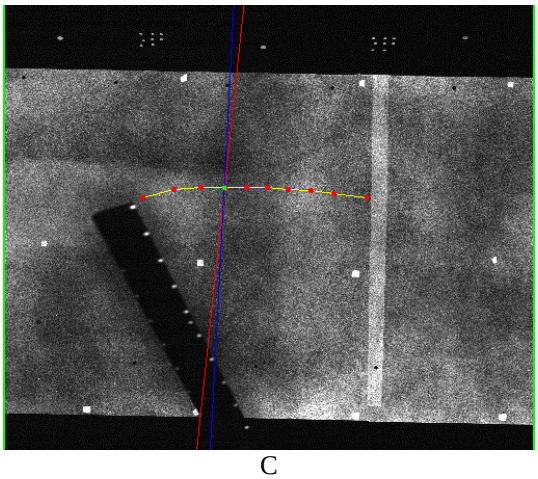

C

Figure 7. Images from cameras A (top), B (bottom-left), and C (bottom-right) showing epipolar lines corresponding to vortex target 4. (The first vortex target is not visible in image B).

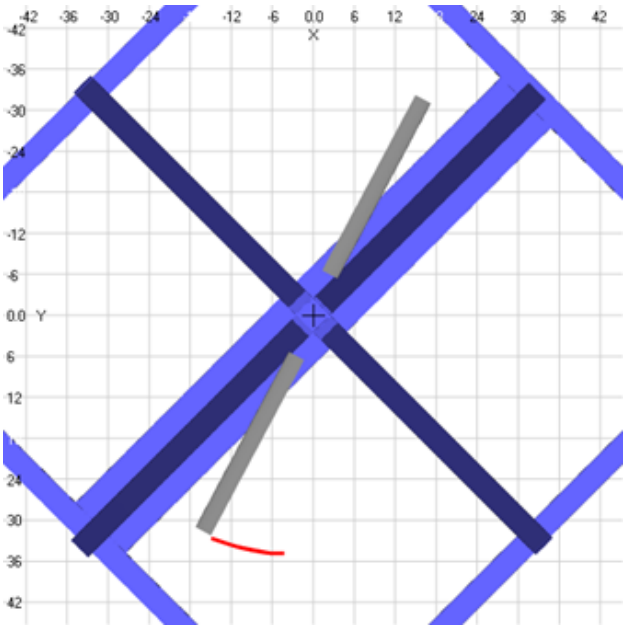

Figure 8. View of rotor and youngest vortex as seen from above. Rotor rotation is clockwise (negative thrust).

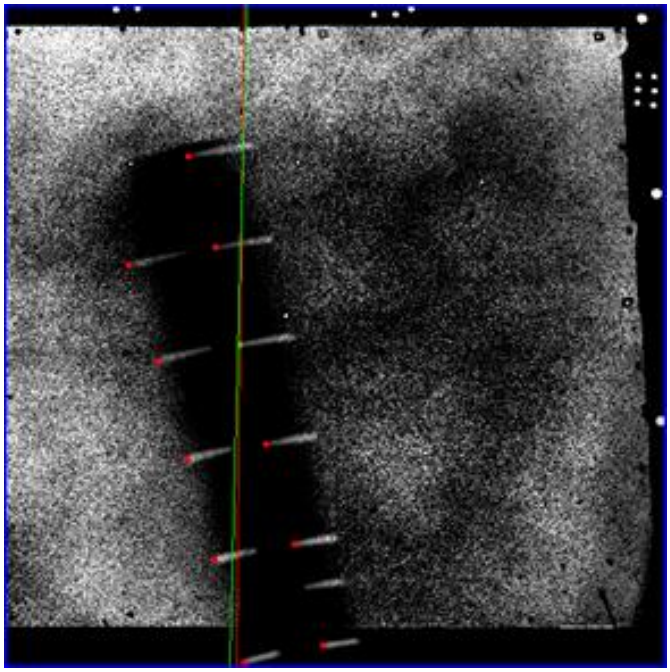

A

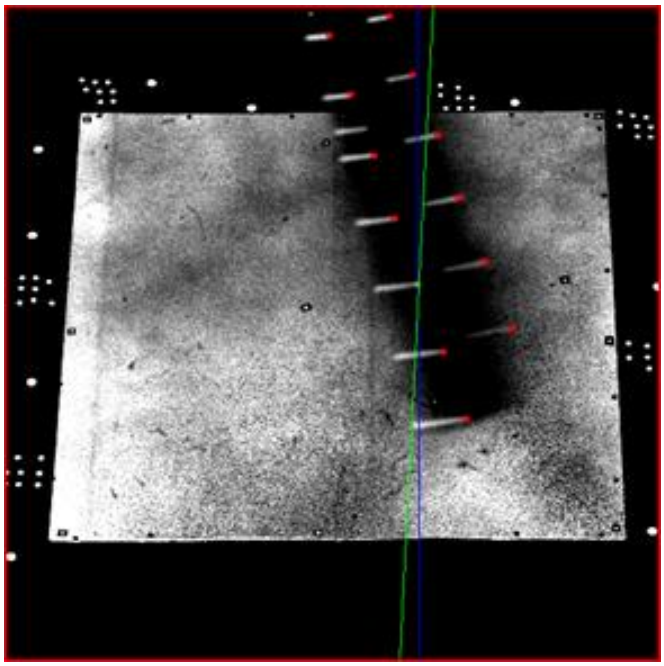

B

Blade Displacement

Figure 9 shows images from the three cameras for the case β = 9 degrees. Targets along the leading and trailing edges are marked. Note that the targets in images from cameras A and B are streaked because during the flash (550 µsec) the rotor tip, travelling at 85 m/sec, advanced 47 mm or 76% of its chord. There was almost no streaking in images from camera C because the flash was much shorter (10 µsec).

In Figure 6, images from cameras A and B include epipolar lines corresponding to the target indicated in the image from camera C. Note that the epipolar lines pass through the end (not the beginning) of the target-streak. This indicates that lamp C was triggered by the trailing edge of the TTL pulse that triggered lamps A and B, not the leading edge as we had first assumed. Thus the flash from lamp C began just as the flashes from lamps A and B ended.

Figure 10 shows the vertical positions of the targets along the trailing edge of the rotor blade plotted versus distance from the rotation axis for the three blade pitch angles. The displacements vary linearly with radial position, and the magnitudes increase with pitch angle. In Figure 8, the angles computed from the difference in the leading and trailing edge targets at each span station are shown. At the two higher pitch angles the measurements are reasonably consistent with the assumed pitch angle. Differences are to be expected because the targets were not precisely at the leading and trailing edges. At the lowest blade angle, targets along the leading edge were difficult to see and thus were located less accurately. This explains the larger scatter in the angle measurements at this condition.

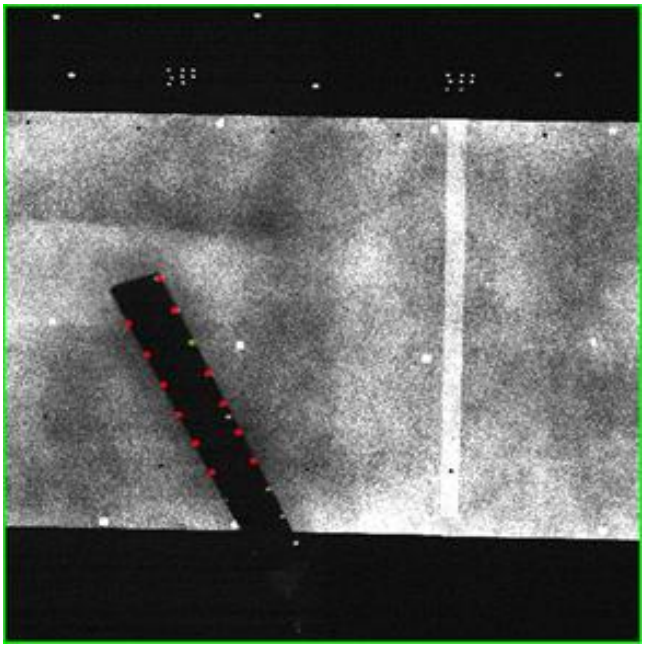

C

Figure 9. Images from cameras A (top-left), B (top-right) and C (bottom) showing epipolar lines corresponding to third target from tip of trailing edge (green marker). As seen from below rotation is counter-clockwise. Note that epipolar lines pass through the end of the target streak in cameras A and B, indicating that camera C was triggered by the trailing edge of the TTL pulse.

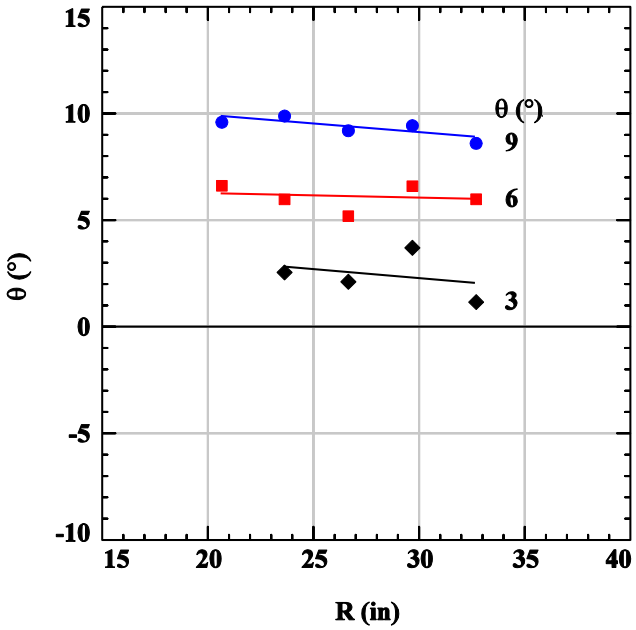

Figure 10. Vertical position of blade trailing-edge targets versus radial position.

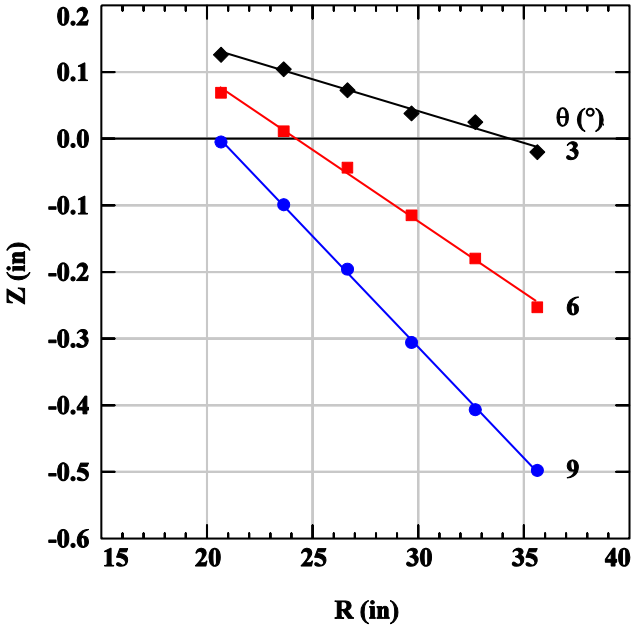

Figure 11. Approximate blade angle computed from leading and trailing edge targets versus radial position.

Mapping Thermography Image Data to Rotor Blade Surface Grid

To transform the thermography data from the image plane to spatial coordinates, a surface grid for the rotor blade was first defined and then mapped to the image using Eq. 1. After this mapping, each node of the surface grid overlay a pixel in the image whose value was then assigned to that point. [The assigned value was actually the area-weighted average of pixels that lay within a 1 x 1 pixel square centered each the node.] To reduce noise, the intensity data were averaged over a spanwise column of 11 pixels centered on each node. Since spanwise variations in intensity were small, this smoothed the data without significantly reducing resolution in the chordwise direction.

The surface grid for the un-deformed rotor blade was easily created knowing the blade chord (65 mm) and radius (900 mm), airfoil section (NACA 0012), taper (0°), and twist (0°). The blade-displacement measurements indicated that blade bending and twist were minimal at the test conditions. Therefore, coordinates of the blade at the test conditions could be approximated by simply rotating the un-deformed surface grid by the blade pitch angle, the rotor cone angle and azimuth angle.

Before the surface grid could be mapped to the images it was necessary to calibrate the thermography camera. It would have been best to do this directly by acquiring images of the calibration structure with the thermography camera, just as for the photogrammetry cameras; however, this was not done. Therefore, the thermography camera was calibrated indirectly using targets on the rotor blades, whose spatial coordinates were measured by the photogrammetry cameras, as calibration targets. The solution for the DLT is ill conditioned when the DLT is computed from a set of targets

that are nearly coplanar (as the rotor-blade targets were at each test condition). Therefore, to avoid this situation, the calibration of the thermal camera was computed by combining target data from all three test conditions, where the cone angles (and out-of-plane positions) of the blades were different.

Figure 12 shows an IR image of the rotor blade at β = 9°. The image is overlaid by chordwise lines of constant span, which were mapped to the image by Eq. 1. In the corner of the figure is a plot of image intensity versus chordwise position at the spanwise station y/b = 0.73. In Figure 13, image intensity data are plotted versus chordwise position at span stations between y/b = 0.6 and 0.9. Figure 14 compares image intensity profiles at span station y / b = 0.8 at the three blade angles.

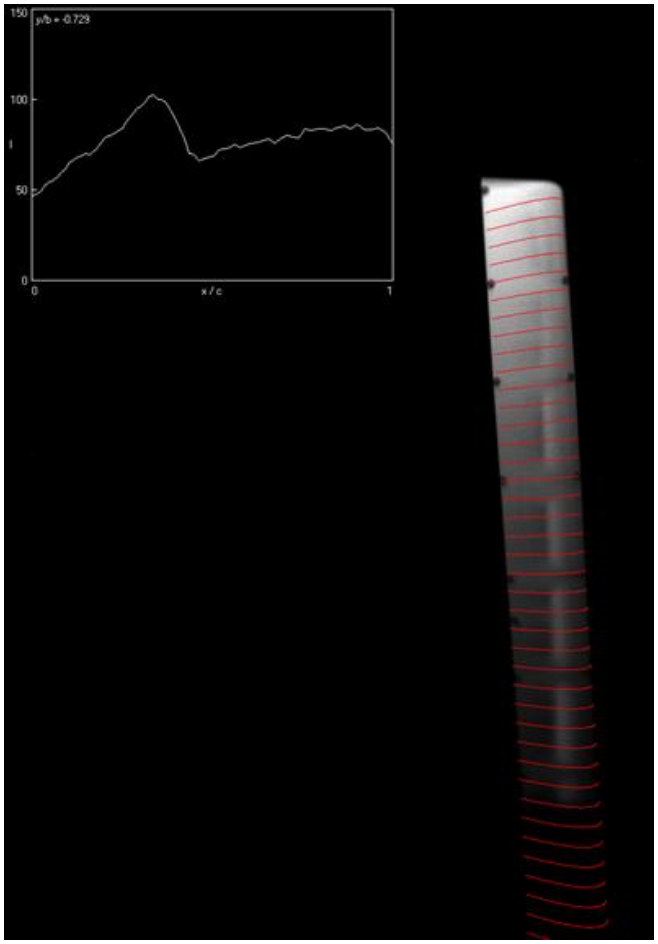

Figure 12. Thermal Image of blade warped to surface grid with inset of an intensity vs. chord plot at y/b of 0.72.

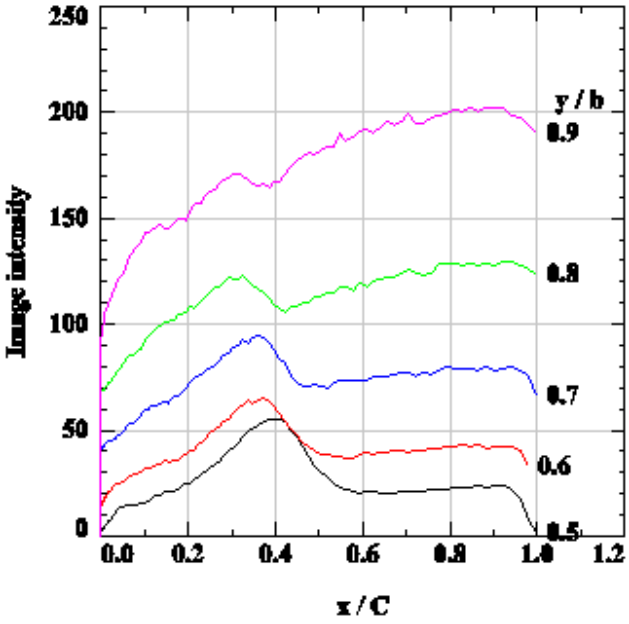

Figure 13. Profile plots of intensity vs. chord location at five spanwise locations

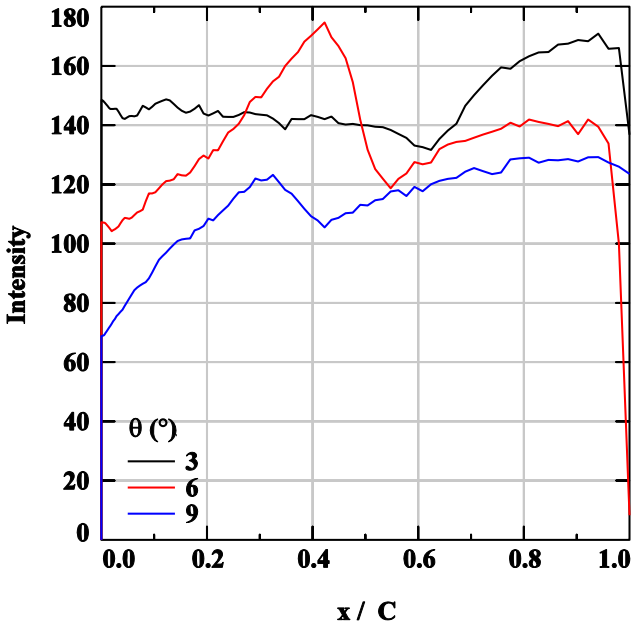

Figure 11. Image intensities along chord-wise line at y / b = 0.8 at three blade angles.

CONCLUSIONS

An experiment to make simultaneous measurements of the boundary-layer transition, blade deformation, vortex filament location and strength was performed at NASA Ames Research center in the Army Hover Chamber was described. The intent of making four separate image-based measurement simultaneously on a one-per-rev basis was achieved, though the TomoPIV measurement proved unusable. Data from the three

other measurements were presented. The advancement of using the photogrammetric calibration from the blade displacement measurement system to the thermal imaging of the boundary layer measurement was described.

ACKNOWLEDGEMENTS

This work was supported by two of NASA's Fundamental Aeronautics research programs: Rotor Wing (Now Revolutionary Vertical Lift Technology – RVLT) and Aerosciences (now Transformational Test Technology - TTT) and the US Army AMERDEC at NASA Ames Research Center. We also want to thank Markus Raffel for participating in the experiment.

REFERENCES

1. Raffel, M., Heineck, J.T., "Mirror based image de-rotation for aerodynamic rotor measurements" AIAA Journal Technical Notes, AIAA JOURNAL Vol. 52, No. 6, June 2014

2. Quast, A., "Detection of Transition by Infrared Image Technique," *Proceedings of the International Congress on Instrumentation in Aerospace Simulation Facilities Record*, Inst. of Electrical and Electronics Engineers, New York, 1987, pp. 125–134

3. L. De Luca, G. Guglieri, G. Cardone, and G. M. Carlomagno. "Experimental analysis of surface flow on a delta wing by infrared thermography", AIAA Journal, Vol. 33, No. 8 (1995), pp. 1510-1512.

4. van Dam, C.P., Shiu, H.J., Banks, D.W., Tracy, R.R., Chase, J., "In-flight visualization of supersonic transition using infrared imaging" *AIAA J. Of Aircraft*, Vol. 39, No. 6, 2002

5. Schairer, E.T., Kushner, L.K., and Heineck, J.T., "Measurements of Tip Vortices from a Full-Scale UH-60A Rotor by Retro-Reflective Background Oriented Schlieren and Stereo Photogrammetry," presented at AHS 69th Annual Forum, Phoenix, AZ, May 21-23, 2013.

6. Geodetic Systems, Inc., http://www.geodetic.com/

7. Abdel-Aziz, Y.I. and Karara, H.M., "Direct Linear Transformation from Comparator Coordinates into Object-Space Coordinates," Proceedings, Symposium on Close-Range Photogrammetry, American Society of Photogrammetry, Urbana, IL, Jan. 1971.

8. Lucas, B.D. and Kanade, T., "An Iterative Image Registration Technique with an Application to Stereo Vision," International Joint Conference on Artificial Intelligence, Aug. 24-28 1981, Vancouver, British Columbia, pp. 674-679.

9. Horn, B.K.P. and Schunck, B.G., "Determining Optical Flow," Artificial Intelligence, 17, 1981, pp. 185-203